THE JOURNAL OF PHYSICAL CHEMISTRY LETTERS
A JOURNAL OF THE AMERICAN CHEMICAL SOCIETY

pubs.acs.org/JPCL Letter

Correlating Interfacial Charge Transfer Rates with Interfacial Molecular Structure in the Tetraphenyldibenzoperiflanthene/C_{70} Organic Photovoltaic System

Jacob Tinnin, Srijana Bhandari, Pengzhi Zhang, Eitan Geva,* Barry D. Dunietz,* Xiang Sun,* and Margaret S. Cheung*

Cite This: J. Phys. Chem. Lett. 2022, 13, 763−769 Read Online

ACCESS | Metrics & More | Article Recommendations | Supporting Information

ABSTRACT: Organic photovoltaics (OPV) is an emerging solar cell technology that offers vast advantages such as low-cost manufacturing, transparency, and solution processability. However, because the performance of OPV devices is still disappointing compared to their inorganic counterparts, better understanding of how controlling the molecular-level morphology can impact performance is needed. To this end, one has to overcome significant challenges that stem from the complexity and heterogeneity of the underlying electronic structure and molecular morphology. In this Letter, we address this challenge in the context of the DBP/C_{70} OPV system by employing a modular workflow that combines recent advances in electronic structure, molecular dynamics, and rate theory. We show how the wide range of interfacial pairs can be classified into four types of interfacial donor−acceptor geometries and find that the least populated interfacial geometry gives rise to the fastest charge transfer (CT) rates.

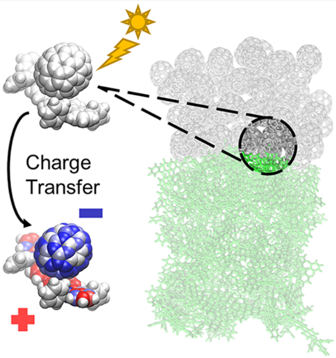

The reduced production and environmental costs as well as improved bandgap tunability and solution processability of organic photovoltaic (OPV) devices compared to those based on conventional inorganic materials are powerful rationales for OPV research.[1−13] The initial step within such OPV devices corresponds to formation of an exciton through photoexcitation. The exciton then diffuses to the interface between donor (D) and acceptor (A) materials, where charge transfer (CT) from a D molecule to an A molecule creates an electron−hole pair.[1−3,14] This pair then undergoes charge separation, where the electron and hole separate and diffuse away from the D/A interface within the A and D matierals, respectively. Successful charge separation leads to collection of the charges at the electrodes and formation of photocurrent. In order to be effective, those primary processes need to occur faster than competing loss processes such as electron−hole recombination.

The amount of charge collected determines the device efficiency. Thus, the rate of the different processes has a direct impact on device performance. OPV performance can be improved by obtaining a molecular level understanding of how variation in the D/A interfacial structure influences CT rate constants.[1,6,15−18]

In this Letter, we investigate the correlation between the interfacial molecular morphology and CT rates in the well-studied OPV system consisting of tetraphenyldibenzoperiflanthene (DBP), as the electron donor, and a fullerene (C_{70}), as the electron acceptor (see Figure 1).[19,20] To this end, we utilize a software package we recently introduced, CTRAMER[21] (**C**harge **T**ransfer **RA**tes from **M**olecular dynamics, **E**lectronic structure, and **R**ate theory), for calculating interfacial CT rates based on molecular dynamics (MD) and electronic structure inputs for interfacial D/A representative geometries. The theoretical framework for calculating CT rate constants is based on the linearized semiclassical Fermi's golden rule (LSC FGR),[22−28] which has an explicit, molecular environment around the D/A pair instead of a polarizable continuum or a harmonic bath.[1,23] The heterogeneity of different interfacial D/A geometries requires this level of atomistic resolution to accurately account for the distribution of CT rates.[1,15,22,29−34]

Our model of the DBP/C_{70} D/A interface consists of 6 alternating layers of DBP and C_{70} with 25 molecules in each layer, which gives rise to a large ensemble of interfacial D/A pair geometries. Analysis of the ensemble of interfacial pair geometries was aided by using cylindrical coordinates (shown in Figure 1c) to represent the location of the center of mass of the C_{70} molecule relative to the center of mass of the DBP molecule. We focused on two order parameters: the distance (Z) from the center of mass of the C_{70} molecule to the center

Received: November 4, 2021
Accepted: January 7, 2022
Published: January 18, 2022

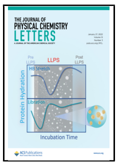

https://doi.org/10.1021/acs.jpclett.1c03618
J. Phys. Chem. Lett. 2022, 13, 763−769

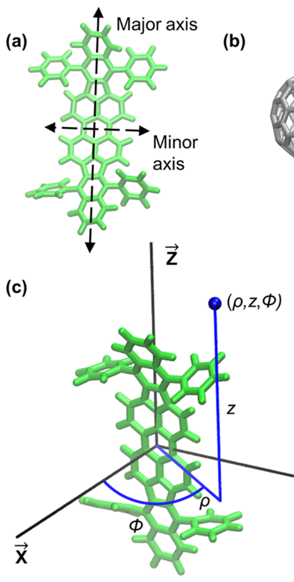

Figure 1. DBP (a) and C_{70} (b) molecules, shown at the same scale, with the cylindrical coordinate system (c) used to define order parameters. Pairs are classified according to the center of mass of C_{70} being "on" (*[1]*) or "off" (*[0]*) the major and minor axes of DBP shown in panel a.

of mass of the DBP molecule projected on the Z axis and the angle of rotation (Φ) for C_{70} around the main axis of DBP.

Figure 2 shows the potential of mean force (PMF) along the order parameters of (*Z*, Φ), (the computational details can be found in the Supporting Information). The free energy landscape is seen to be relatively flat with variations of less than 2 *kT*. The region of highest probability, located at (0 Å, 0°), had previously been identified as energetically most favorable[19] but was found here to comprise only a small fraction of the ensemble. Other low-energy regions are centered at (0 Å, 70°) and a long vertical region with basins centered at (9 Å, 0°) and (12 Å, 60°). The ridgelines shown in Figure 2 divide each of these basins at the crests of highest energy between them using a density-based clustering algorithm.

The four basins reflect the symmetry of the DBP molecule defined by a long major axis and a shorter minor axis. We utilized a *major*−*minor* naming scheme that references the position of the C_{70} molecule on a given axis as *[1]* and off the axis as *[0]*. The representative structures for these basins were therefore referred to as *[1,1]*, *[0,1]*, *[1,0]*, and *[0,0]*. Figure 1b shows that most interfacial D/A pairs (61%) are found in the *[0,0]* geometry. The D/A pair geometry with the highest probability in each region was selected to represent the entire region for CT rate analysis.

Excited-state calculations at the representative D/A geometries were performed based on a screened-range-separated hybrid (SRSH) functional[30,35−37] based on the Perdew−Burke−Erzenhof (PBE) functional[38−40] (see further details in Computational Methods). Each state is characterized by the (1) excitation energy of the D/A pair (*E*), (2) oscillator strength (OS) of the pair,[41] and (3) donor molecule's charge (Q_D). These properties of the excited states are shown in Figure 3.

Each geometry contains a similar number of dark CT (dCT) states (18, 16, 20, and 16 dCT states for *[1,1]*, *[0,1]*, *[1,0]*, and *[0,0]*, respectively) and a single bright state denoted as EX1. The OS of the EX1 state for the *[1,1]* geometry (0.94) was lower than the OS of the EX1 states for the *[0,1]*, *[1,0]*, and *[0,0]* geometries (1.24, 1.17, and 1.46) as shown in Figure 3.

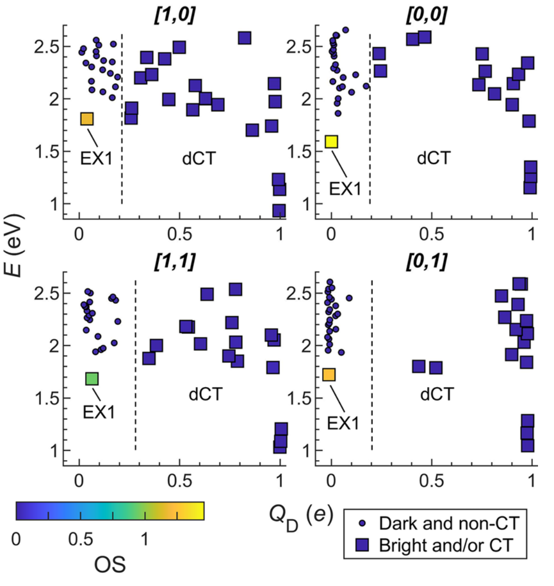

Figure 2. Potential of mean force for the DBP/C_{70} pair using a *Z*−Φ cylindrical coordinate system. Also shown are representative structures of DBP/C_{70} pair at each of the four geometries (*[1,1]*, *[0,1]*, *[1,0]*, and *[0,0]*). *Z* is the distance of the C_{70} along the main axis of the DBP molecule from its center, and Φ is the angle of rotation around the main axis (see Figure 1c). The percentage of sampled pairs corresponding to each representative structure is listed next to their label. Solid black lines show the border of each region.

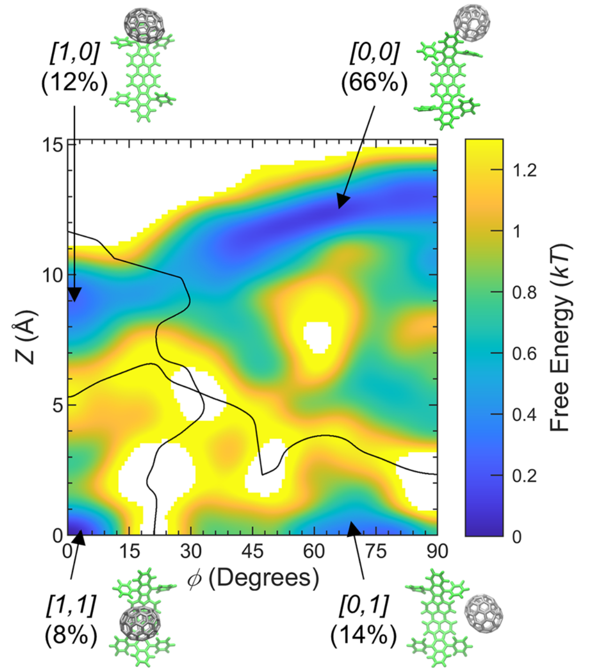

Figure 3. Scatter plot of the donor/acceptor pair's excitation energy (*E*) versus the donor molecule's charge (Q_D) for the 40 lowest-energy excited states of each representative geometry. Each dot is shaded based on its oscillator strength (OS). States involved in the CT process are represented by large squares, while other states are shown by smaller circles.

The excitation energies for all four EX1 states are around 1.7 eV. Similarly, the excitation energies of the dCT states are similar across the four geometries. The dCT states for *[0,1]* and *[0,0]* mostly corresponded to the charge transfer of roughly a full electron, whereas several dCT states for *[1,1]* and *[1,0]* had significantly smaller values of Q_D. Numerical values represented in Figure 3 can be found in Table S2.

Next, we compute the electron transfer rate constant, k^M, for donor state (EX1) to acceptor state (dCT*n*) transitions at the Marcus level, which is computed using the mean and variance of the energy gap between donor and acceptor states as obtained from all-atom MD simulations.[21] We note that the condensed-phase polarizable environment is expected to stabilize CT states more than localized excitations do.[29]

As shown in Figure 4, transitions with large k^M are found in all geometries, with *[1,1]* having six of the seven transitions over 10^{12} Hz. The EX1 → dCT10 transition from the *[1,1]* geometry had the fastest k^M by a factor of 5, which is due to having both a very small energy gap and the largest coupling. This resulted in the *[1,1]* geometry having the largest overall CT rate (shown in Figure 4 and Table 1), represented by K^C as defined in eq 3. The K^C for each of the other geometries was only an order of magnitude lower. The difference in contribution to CT rate density (ω^C), defined in eq 4, between *[1,1]* and the other geometries is even smaller because of the small population of the *[1,1]* geometry.

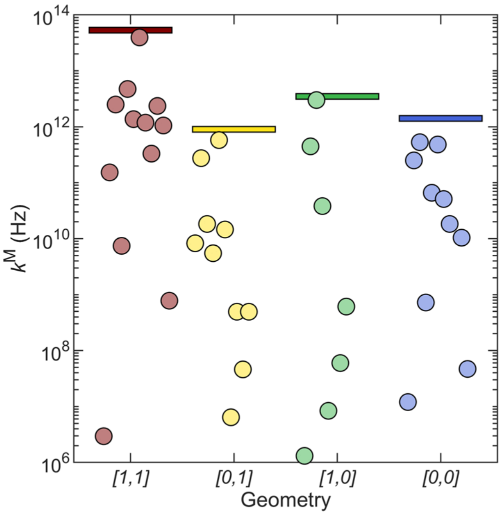

Figure 4. Charge transfer rate constants (k^M) for the donor-to-acceptor transition in each representative geometry. Each dot represents a single transition (e.g., EX1 → dCT10). The thin rectangles correspond to the total rate (K^M) for each geometry. The spacing on the x axis is offset to allow for easier resolution of each point. Values for each transition are recorded in Table S1.

Table 1. Charge Transfer Rate, K^C, and Rate Densities, ω^C, for Representative Geometries

Geometry	Percent of Interface	K^C (nA)	ω^C (nA/nm²)
[1,1]	8.2±0.1%	5520±382	931±65
[0,1]	13.9±0.1%	140± 6	40± 2
[1,0]	12.2±0.1%	503± 52	126±13
[0,0]	65.7±0.1%	206± 3	279± 4
Total	**100%**		**1377±67**

Hundreds of thousands of D/A pairs were sampled from MD simulations of the DBP/C_{70} interface. Classifying the different pair geometries based on the cylindrical coordinates as shown in Figure 1c resulted in several clustered regions. Each region corresponds to the placement of the C_{70} molecule "on" (*[1]*) or "*off*" (*[0]*) the major and minor axis of the DBP molecule (see Figure 1a). While the *[1,1]* geometry was the most energetically favorable, Figure 2 shows that it corresponds to the narrowest basis and therefore the smallest subpopulation. In contrast, the *[0,0]* geometry corresponds to the widest basis and as a result the largest subpopulation (over half the D/A pairs).

A representative pair was chosen for each cluster in $Z-\Phi$ space followed by calculating its excited states using TD-DFT and CT rate constants, with k^M corresponding to transition between excited states. By summing k^M for each transition of a geometry and accounting for the quantity of charge transferred, we obtained an overall CT rate constant, K^C. Table 1 shows that the *[1,1]* geometry had the highest K^C by an order of magnitude. This higher K^C is likely due to the higher contact area between DBP and C_{70} that comes from being "*on*" both axes. Each of the other three geometries had a similar K^C. Future studies can use CTRAMER to study the variance of K^C within each region.

At the same time, the overall low population of the *[1,1]* geometry limited its impact on the overall CT efficiency. To measure this, we used CT rate density, ω^C, which accounts for both the CT rate and the prevalence of a geometry. Table 1 shows that *[1,1]* still has the largest impact on system-level CT, despite its relatively low population. This result suggests that changes in device fabrication that affect the relative population of these geometries has the potential to have a large impact on device performance. *[1,1]* was the most favorable geometry for CT; however, its low population leaves room for optimization in the fabrication procedure. The greater population of the other geometries allowed them to also have a significant impact on overall CT efficiency.

These results show that a condensed-phase interface can stabilize multiple geometries that have both a significant population and a fast CT rate. This illustrates the need for a multiscale software like CTRAMER, which handles complex many-body effects with MD and the sophisticated electronic structure methods needed to accurately calculate excited-state properties. Our results suggest that small changes in the molecular morphology of DBP/C_{70} can have large effects on device performance.

■ COMPUTATIONAL METHODS

The overall computational workflow is outlined in Figure 5. The electronic structure calculations (represented in Figure 5a,b,f,g) were performed using Q-Chem 5.[42] Time-dependent density-functional theory (TD-DFT) was used on interfacial D/A molecule pairs selected from MD simulations in order to calculate excited states as well as their oscillator strength (OS), partial charges, and relative energy.[43] Specific parameter choices used to implement the calculations are given in the Supporting Information.

The states were then classified as bright (light absorbing) and/or CT states using the following criteria. First, CT states were defined as states where the donor molecule's charge, Q_D, was greater than 0.25*e*. Second, bright states were defined as the states with highest OS.[41] Bright, non-CT states were denoted by EX (excitonic), while CT states were denoted by

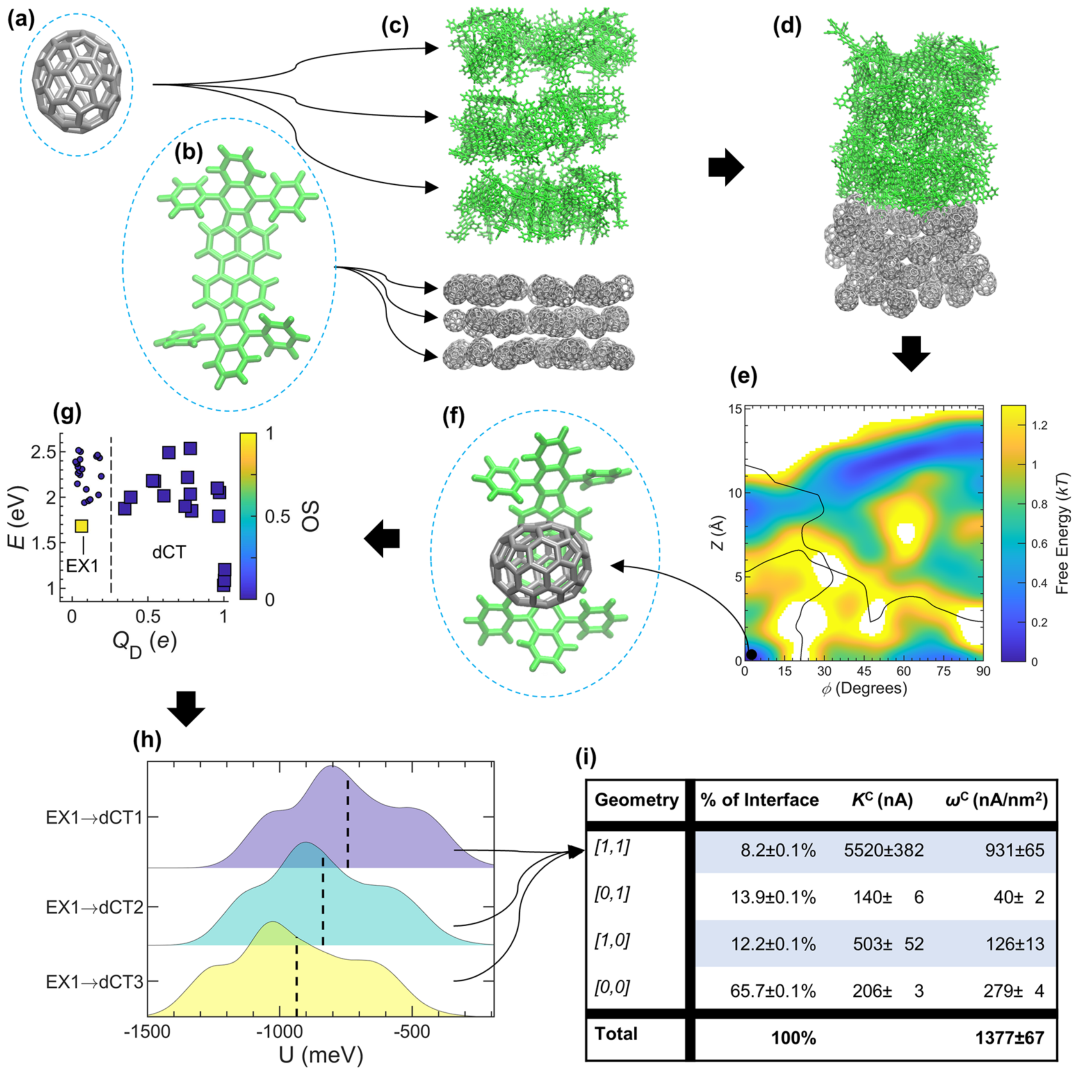

Geometry	% of Interface	K^C (nA)	ω^C (nA/nm²)
[1,1]	8.2±0.1%	5520±382	931±65
[0,1]	13.9±0.1%	140± 6	40± 2
[1,0]	12.2±0.1%	503± 52	126±13
[0,0]	65.7±0.1%	206± 3	279± 4
Total	**100%**		**1377±67**

Figure 5. Overall workflow of calculations in this Letter. (a and b) First, DFT calculations were performed on the C_{70} and DBP molecules separately, as represented by the blue ovals. (c) Next, the atomic coordinates and Mulliken charges from panels a and b were used to construct a condensed-phase system. (d) Then, the system from panel c was equilibrated and (e) the potential of mean force was obtained using MD. (f) DBP/C_{70} pairs were then selected from panel e, and excited states were calculated using TD-DFT and (g) classified using CTRAMER. (h) Energy gap distributions between donor and acceptor states were calculated using MD for use in computing (i) charge transfer rate constants and rate densities.

dCT (dark CT) as no bright, CT states were found. Each individual state was then classified as EX*n* or dCT*n*, where *n* represents the rank of that state's energy, from smallest to largest, of states with the same type and geometry. Transitions were then selected using each possible combination of a bright state and a CT state. The electronic coupling coefficients of each transition were computed via the fragment-charge-differences (FCD) method.[44]

Condensed-phase systems of 150 molecules were constructed using Packmol (shown in Figure 5c) using 6 square layers.[45] The SANDER[46] program from AMBER12 was used for MD simulations as detailed in the Supporting Information (shown in Figure 5d). Six parallel runs of 5 ns each were used. DBP/C_{70} pairs were sampled from the MD production runs with interfacial D/A pair defined as 1 DBP and 1 C_{70} where the displacement between the closest atoms from separate molecules was smaller than 5 Å. Each D/A pair was then characterized using a cylindrical coordinate system as shown in Figure 1c and Figure 5e for the C_{70} center of mass with the origin at the DBP center of mass. To utilize the symmetry of DBP, points were reflected such that $Z \in [0\text{ Å}, \infty\text{ Å})$ and $\Phi \in [0°, 90°]$. Details of calculating the energy landscape are given in the Supporting Information.

Production runs for rate calculations included the entire system surrounding the selected D/A pair which was assigned its partial charge from TD-DFT and restrained to its geometry using a protocol detailed in the Supporting Information. All other molecules kept ground-state charges and were unrestrained. All other parameters were the same as for MD simulations for population analysis. For each transition 5 parallel runs of 5 ns were used.

A Marcus-level expression derived from LSC FGR[1,23−27] was then used to calculate the transition rate constant (k^M) from donor state to acceptor state, where

$$k^M = \frac{|\Gamma_{DA}|^2}{\hbar}\sqrt{\frac{2\pi}{\sigma_U^2}}\exp\left[-\frac{U^2}{2\sigma_U^2}\right] \tag{1}$$

Here, $U(\mathbf{R}) = V_D(\mathbf{R}) - V_A(\mathbf{R})$ is the energy gap between donor and acceptor states (shown in Figure 5h) where V_D and V_A are the potential-energy surfaces of the donor and acceptor states, respectively, and $\mathbf{R}$ represents the nuclear coordinates. $\langle U\rangle$ and σ_U are the mean and variance, respectively, of $U(\mathbf{R})$. To relate this "Marcus-level" expression with the traditional Marcus formula,[47,48] the reorganization energy (E_r), the reaction free energy (ΔE), and the activation energy (E_a) can be calculated from $\langle U\rangle$ and σ_U: $E_r = \sigma_U^2/(2k_BT)$, $\Delta E = -E_r - \langle U\rangle$, and $E_a = k_BT\langle U\rangle^2/(2\sigma_U^2)$.[49−52] Parameters for calculating k^M are given in the Supporting Information.

While k^M is a rate constant for transition between states, we multiplied it by the amount of the charge transferred during that transition, (ΔQ_D), to obtain a CT rate constant (k^C):

$$k^C = \Delta Q_D k^M \tag{2}$$

While both k^C and k^M can be used to compare the rates of different transitions, to compare the efficiency of different structures a structure-level CT rate constant (shown in Figure 5i) is needed. We summed k^C over each transition, t, from each representative structure, i, to get this structure-level CT rate constant:

$$K_i^C = \sum_t k_t^C \tag{3}$$

A system-level CT rate density (ω^C) was then similarly obtained using an average of K_i^C, weighted by the average population (n_i) of each structure (i), divided by the average area (A) of the D/A interface in the simulation (41 nm^2):

$$\omega^C = \sum_i (K_i^C n_i) \times \frac{1}{A} \tag{4}$$

■ ASSOCIATED CONTENT

SI Supporting Information

The Supporting Information is available free of charge at https://pubs.acs.org/doi/10.1021/acs.jpclett.1c03618.

> A table of CT rate parameters, a table of excited-state properties, and energy correction terms for each state; additional computational details for reproducibility (PDF)

■ AUTHOR INFORMATION

Corresponding Authors

Eitan Geva − *Department of Chemistry, University of Michigan, Ann Arbor, Michigan 48109, United States;* orcid.org/0000-0002-7935-4586; Email: eitan@umich.edu

Barry D. Dunietz − *Department of Chemistry and Biochemistry, Kent State University, Kent, Ohio 44242, United States;* orcid.org/0000-0002-6982-8995; Email: bdunietz@kent.edu

Xiang Sun − *Division of Arts and Sciences, NYU Shanghai, Shanghai 200122, China; NYU-ECNU Center for Computational Chemistry, NYU Shanghai, Shanghai 200062, China; Department of Chemistry, New York University, New York, New York 10003, United States;* orcid.org/0000-0002-2846-8532; Email: xiang.sun@nyu.edu

Margaret S. Cheung − *Department of Physics, University of Houston, Houston, Texas 77204, United States; Center for Theoretical Biological Physics, Rice University, Houston, Texas 77030-1402, United States; Environmental Molecular Sciences Laboratory, Pacific Northwest National Laboratory, Richland, Washington 99354, United States;* orcid.org/0000-0001-9235-7661; Email: margaret.cheung@pnnl.gov

Authors

Jacob Tinnin − *Department of Physics, University of Houston, Houston, Texas 77204, United States; Center for Theoretical Biological Physics, Rice University, Houston, Texas 77030-1402, United States*

Srijana Bhandari − *Department of Chemistry and Biochemistry, Kent State University, Kent, Ohio 44242, United States; Department of Chemistry, Case Western Reserve University, Cleveland, Ohio 44106, United States*

Pengzhi Zhang − *Department of Physics, University of Houston, Houston, Texas 77204, United States*

Complete contact information is available at: https://pubs.acs.org/10.1021/acs.jpclett.1c03618

Notes

The authors declare no competing financial interest.

■ ACKNOWLEDGMENTS

E.G., B.D.D., and M.S.C. acknowledge support from the Department of Energy (DOE), Basic Energy Sciences through the Chemical Sciences, Geosciences and Biosciences Division (No. DE-SC0016501). X.S. acknowledges support from the National Natural Science Foundation of China (No. 21903054) and the Program for Eastern Young Scholar at Shanghai Institutions of Higher Learning. Computational resources are provided by the National Energy Research Scientific Computing Center (NERSC), a U.S. Department of Energy Office of Science User Facility operated under Contract No. DE-AC02-05CH11231, as well as the uHPC cluster managed by the University of Houston and acquired through NSF Award Number OAC 1531814.

■ REFERENCES

(1) Tinnin, J.; Bhandari, S.; Zhang, P.; Aksu, H.; Maiti, B.; Geva, E.; Dunietz, B. D.; Sun, X.; Cheung, M. S. Molecular-Level Exploration of the Structure-Function Relations Underlying Interfacial Charge Transfer in the Subphthalocyanine/C60 Organic Photovoltaic System. *Phys. Rev. Appl.* **2020**, *13* (5), 11.

(2) Lee, M. H.; Geva, E.; Dunietz, B. D. Calculation from First-Principles of Golden Rule Rate Constants for Photoinduced Subphthalocyanine/Fullerene Interfacial Charge Transfer and Recombination in Organic Photovoltaic Cells. *J. Phys. Chem. C* **2014**, *118* (18), 9780−9789.

(3) Zhao, Y.; Liang, W. Charge transfer in organic molecules for solar cells: theoretical perspective. *Chem. Soc. Rev.* **2012**, *41* (3), 1075−1087.

(4) Kim, J.; Yim, S. Influence of surface morphology evolution of SubPc layers on the performance of SubPc/C-60 organic photovoltaic cells. *Appl. Phys. Lett.* **2011**, *99* (19), 193303.

(5) Tian, H.; Yu, Z.; Hagfeldt, A.; Kloo, L.; Sun, L. Organic Redox Couples and Organic Counter Electrode for Efficient Organic Dye-Sensitized Solar Cells. *J. Am. Chem. Soc.* **2011**, *133* (24), 9413−9422.

(6) Tong, X.; Lassiter, B. E.; Forrest, S. R. Inverted organic photovoltaic cells with high open-circuit voltage. *Org. Electron.* **2010**, *11* (4), 705−709.

(7) Hagfeldt, A.; Boschloo, G.; Sun, L.; Kloo, L.; Pettersson, H. Dye-Sensitized Solar Cells. *Chem. Rev.* **2010**, *110* (11), 6595−6663.

(8) Wang, T.; Bredas, J.-L. Organic Solar Cells Based on Non-fullerene Small-Molecule Acceptors: Impact of Substituent Position. *Matter* **2020**, *2* (1), 119−135.

(9) Kurpiers, J.; Ferron, T.; Roland, S.; Jakoby, M.; Thiede, T.; Jaiser, F.; Albrecht, S.; Janietz, S.; Collins, B. A.; Howard, I. A.; et al. Probing the pathways of free charge generation in organic bulk heterojunction solar cells. *Nat. Commun.* **2018**, *9* (1), 2038.

(10) Falke, S. M.; Rozzi, C. A.; Brida, D.; Maiuri, M.; Amato, M.; Sommer, E.; De Sio, A.; Rubio, A.; Cerullo, G.; Molinari, E.; et al. Coherent ultrafast charge transfer in an organic photovoltaic blend. *Science* **2014**, *344* (6187), 1001−1005.

(11) Benatto, L.; Marchiori, C. F. N.; Talka, T.; Aramini, M.; Yamamoto, N. A. D.; Huotari, S.; Roman, L. S.; Koehler, M. Comparing C-60 and C-70 as acceptor in organic solar cells: Influence of the electronic structure and aggregation size on the photovoltaic characteristics. *Thin Solid Films* **2020**, *697*, 137827.

(12) Giebink, N. C.; Wiederrecht, G. P.; Wasielewski, M. R.; Forrest, S. R. Ideal diode equation for organic heterojunctions. I. Derivation and application. *Phys. Rev. B* **2010**, *82* (15), 155305.

(13) Giebink, N. C.; Wiederrecht, G. P.; Wasielewski, M. R.; Forrest, S. R. Thermodynamic efficiency limit of excitonic solar cells. *Phys. Rev. B* **2011**, *83* (19), 195326.

(14) Lee, M. H.; Dunietz, B. D.; Geva, E. Donor-to-Donor vs Donor-to-Acceptor Interfacial Charge Transfer States in the Phthalocyanine-Fullerene Organic Photovoltaic System. *J. Phys. Chem. Lett.* **2014**, *5* (21), 3810−3816.

(15) Balamurugan, D.; Aquino, A. J. A.; de Dios, F.; Flores, L.; Lischka, H.; Cheung, M. S. Multiscale Simulation of the Ground and Photo-Induced Charge-Separated States of a Molecular Triad in Polar Organic Solvent: Exploring the Conformations, Fluctuations, and Free Energy Landscapes. *J. Phys. Chem. B* **2013**, *117* (40), 12065−12075.

(16) Brédas, J.-L.; Beljonne, D.; Coropceanu, V.; Cornil, J. Charge-Transfer and Energy-Transfer Processes in π-Conjugated Oligomers and Polymers: A Molecular Picture. *Chem. Rev.* **2004**, *104* (11), 4971−5004.

(17) D'Innocenzo, V.; Grancini, G.; Alcocer, M. J. P.; Kandada, A. R. S.; Stranks, S. D.; Lee, M. M.; Lanzani, G.; Snaith, H. J.; Petrozza, A. Excitons versus free charges in organo-lead tri-halide perovskites. *Nat. Commun.* **2014**, *5* (1), 3586.

(18) Tang, C. W.; VanSlyke, S. A. Organic Electroluminescent Diodes. *Appl. Phys. Lett.* **1987**, *51* (51), 913.

(19) Song, Y.; Schubert, A.; Liu, X.; Bhandari, S.; Forrest, S. R.; Dunietz, B. D.; Geva, E.; Ogilvie, J. P. Efficient Charge Generation via Hole Transfer in Dilute Organic Donor−Fullerene Blends. *J. Phys. Chem. Lett.* **2020**, *11* (6), 2203−2210.

(20) Xiao, X.; Zimmerman, J. D.; Lassiter, B. E.; Bergemann, K. J.; Forrest, S. R. A hybrid planar-mixed tetraphenyldibenzoperiflanthene/C-70 photovoltaic cell. *Appl. Phys. Lett.* **2013**, *102* (7), 073302.

(21) Tinnin, J.; Aksu, H.; Tong, Z.; Zhang, P.; Geva, E.; Dunietz, B. D.; Sun, X.; Cheung, M. S. CTRAMER: An open-source software package for correlating interfacial charge transfer rate constants with donor/acceptor geometries in organic photovoltaic materials. *J. Chem. Phys.* **2021**, *154* (21), 214108.

(22) Sun, X.; Zhang, P.; Lai, Y.; Williams, K. L.; Cheung, M. S.; Dunietz, B. D.; Geva, E. Computational Study of Charge-Transfer Dynamics in the Carotenoid-Porphyrin-C-60 Molecular Triad Solvated in Explicit Tetrahydrofuran and Its Spectroscopic Signature. *J. Phys. Chem. C* **2018**, *122* (21), 11288−11299.

(23) Sun, X.; Geva, E. Equilibrium Fermi's Golden Rule Charge Transfer Rate Constants in the Condensed Phase: The Linearized Semiclassical Method vs Classical Marcus Theory. *J. Phys. Chem. A* **2016**, *120* (19), 2976−2990.

(24) Hu, Z.; Tong, Z.; Cheung, M. S.; Dunietz, B. D.; Geva, E.; Sun, X. Photoinduced Charge Transfer Dynamics in the Carotenoid-Porphyrin-C-60 Triad via the Linearized Semiclassical Nonequilibrium Fermi's Golden Rule. *J. Phys. Chem. B* **2020**, *124* (43), 9579−9591.

(25) Sun, X.; Geva, E. Nonequilibrium Fermi's Golden Rule Charge Transfer Rates via the Linearized Semiclassical Method. *J. Chem. Theory Comput.* **2016**, *12* (6), 2926−2941.

(26) Sun, X.; Geva, E. Non-Condon equilibrium Fermi's golden rule electronic transition rate constants via the linearized semiclassical method. *J. Chem. Phys.* **2016**, *144* (24), 244105.

(27) Sun, X.; Geva, E. Non-Condon nonequilibrium Fermi's golden rule rates from the linearized semiclassical method. *J. Chem. Phys.* **2016**, *145* (6), 064109.

(28) Tong, Z.; Gao, X.; Cheung, M. S.; Dunietz, B. D.; Geva, E.; Sun, X. Charge transfer rate constants for the carotenoid-porphyrin-C-60 molecular triad dissolved in tetrahydrofuran: The spin-boson model vs the linearized semiclassical approximation. *J. Chem. Phys.* **2020**, *153* (4), 044105.

(29) Manna, A. K.; Balamurugan, D.; Cheung, M. S.; Dunietz, B. D. Unraveling the Mechanism of Photoinduced Charge Transfer in Carotenoid-Porphyrin-C-60 Molecular Triad. *J. Phys. Chem. Lett.* **2015**, *6* (7), 1231−1237.

(30) Aksu, H.; Schubert, A.; Geva, E.; Dunietz, B. D. Explaining Spectral Asymmetries and Excitonic Characters of the Core Pigment Pairs in the Bacterial Reaction Center Using a Screened Range-Separated Hybrid Functional. *J. Phys. Chem. B* **2019**, *123* (42), 8970−8975.

(31) Steffen, M. A.; Lao, K.; Boxer, S. G. Dielectric Asymmetry in the Photosynthetic Reaction-Center. *Science* **1994**, *264* (5160), 810−816.

(32) Niedringhaus, A.; Policht, V. R.; Sechrist, R.; Konar, A.; Laible, P. D.; Bocian, D. F.; Holten, D.; Kirmaier, C.; Ogilvie, J. P. Primary processes in the bacterial reaction center probed by two-dimensional electronic spectroscopy. *Proc. Natl. Acad. Sci. U. S. A.* **2018**, *115* (14), 3563−3568.

(33) Koepke, J.; Krammer, E. M.; Klingen, A. R.; Sebban, P.; Ullmann, G. M.; Fritzsch, G. pH modulates the quinone position in the photosynthetic reaction center from Rhodobacter sphaeroides in the neutral and charge separated states. *J. Mol. Biol.* **2007**, *371* (2), 396−409.

(34) Brian, D.; Sun, X. Charge-Transfer Landscape Manifesting the Structure−Rate Relationship in the Condensed Phase Via Machine Learning. *J. Phys. Chem. B* **2021**, *125* (48), 13267−13278.

(35) Refaely-Abramson, S.; Sharifzadeh, S.; Jain, M.; Baer, R.; Neaton, J. B.; Kronik, L. Gap renormalization of molecular crystals from density-functional theory. *Phys. Rev. B* **2013**, *88* (8), 081204.

(36) Zheng, Z.; Egger, D. A.; Brédas, J.-L.; Kronik, L.; Coropceanu, V. Effect of Solid-State Polarization on Charge-Transfer Excitations and Transport Levels at Organic Interfaces from a Screened Range-Separated Hybrid Functional. *J. Phys. Chem. Lett.* **2017**, *8* (14), 3277−3283.

(37) Lüftner, D.; Refaely-Abramson, S.; Pachler, M.; Resel, R.; Ramsey, M. G.; Kronik, L.; Puschnig, P. Experimental and theoretical electronic structure of quinacridone. *Phys. Rev. B* **2014**, *90* (7), 075204.

(38) Ernzerhof, M.; Scuseria, G. E. Assessment of the Perdew−Burke−Ernzerhof exchange-correlation functional. *J. Chem. Phys.* **1999**, *110* (11), 5029−5036.

(39) Paier, J.; Hirschl, R.; Marsman, M.; Kresse, G. The Perdew−Burke−Ernzerhof exchange-correlation functional applied to the G2−1 test set using a plane-wave basis set. *J. Chem. Phys.* **2005**, *122* (23), 234102.

(40) Perdew, J. P.; Burke, K.; Ernzerhof, M. Generalized Gradient Approximation Made Simple. *Phys. Rev. Lett.* **1996**, *77* (18), 3865−3868.

(41) Robinson, J. W. *Atomic Spectroscopy*, 2nd ed.; Marcel Dekker, Inc.: New York, 1996.

(42) Shao, Y.; Molnar, L. F.; Jung, Y.; Kussmann, J.; Ochsenfeld, C.; Brown, S. T.; Gilbert, A. T. B.; Slipchenko, L. V.; Levchenko, S. V.; O'Neill, D. P.; et al. Advances in methods and algorithms in a modern quantum chemistry program package. *Phys. Chem. Chem. Phys.* **2006**, *8* (27), 3172−3191.

(43) Runge, E.; Gross, E. K. U. Density-Functional Theory for Time-Dependent Systems. *Phys. Rev. Lett.* **1984**, *52* (12), 997−1000.

(44) Voityuk, A. A.; Rosch, N. Fragment charge difference method for estimating donor-acceptor electronic coupling: Application to DNA pi-stacks. *J. Chem. Phys.* **2002**, *117* (12), 5607−5616.

(45) Martinez, L.; Andrade, R.; Birgin, E. G.; Martinez, J. M. PACKMOL: A Package for Building Initial Configurations for Molecular Dynamics Simulations. *J. Comput. Chem.* **2009**, *30* (13), 2157−2164.

(46) Case, D. A.; Darden, T. A.; T.E. Cheatham, I.; Simmerling, C. L.; Wang, J.; Duke, R. E.; Luo, R.; Walker, R. C.; Zhang, W.; Merz, K. M., et al. *AMBER 12*; University of California: San Francisco, 2012.

(47) Cao, J.; Jung, Y. Spectral analysis of electron transfer kinetics. I. Symmetric reactions. *J. Chem. Phys.* **2000**, *112* (10), 4716−4722.

(48) Cao, J.; Voth, G. A. A unified framework for quantum activated rate processes. II. The nonadiabatic limit. *J. Chem. Phys.* **1997**, *106* (5), 1769−1779.

(49) Barbara, P. F.; Meyer, T. J.; Ratner, M. A. Contemporary issues in electron transfer research. *J. Phys. Chem.* **1996**, *100* (31), 13148−13168.

(50) Marcus, R. A. On the Theory of Oxidation-Reduction Reactions Involving Electron Transfer. *J. Chem. Phys.* **1956**, *24* (5), 966−978.

(51) Marcus, R. A. Electrostatic Free Energy and Other Properties of States Having Nonequilibrium Polarization. *J. Chem. Phys.* **1956**, *24* (5), 979−989.

(52) Marcus, R. A. Electron-Transfer Reactions in Chemistry - Theory and Experiment. *Rev. Mod. Phys.* **1993**, *65* (3), 599−610.